Cubic $NaSbS_2$ as an Ionic-Electronic Coupled Semiconductor for Switchable Photovoltaic and Neuromorphic Device Applications

P.C. Harikesh, Abhijith Surendran†, Biplab Ghosh†, Rohit Abraham John†, Arjun Moorthy, Natalia Yantara, Teddy Salim, Krishnamoorthy Thirumal, Wei Lin Leong, Subodh Mhaisalkar, Nripan Mathews*

† Contributed equally

P.C. Harikesh, Biplab Ghosh, Arjun Moorthy, Dr. Natalia Yantara, Krishnamoorthy Thirumal, Prof. Wei Lin Leong, Prof. Subodh Mhaisalkar, Prof. Nripan Mathews*

Energy Research Institute @NTU (ERI@N), Research Techno Plaza, X-Frontier Block, Level 5, 50 Nanyang Drive, 637553 Singapore.

Email: Nripan@ntu.edu.sg

P.C. Harikesh

Interdisciplinary Graduate School, Energy Research Institute at NTU, 639798 Singapore

Abhijith Surendran, Prof. Wei Lin Leong

School of Electrical and Electronic Engineering, Nanyang Technological University, 50 Nanyang Avenue, Singapore 639798, Singapore

Dr. Rohit Abraham John, Dr. Teddy Salim, Prof. Subodh Mhaisalkar, Prof. Nripan Mathews

School of Materials Science and Engineering, Nanyang Technological University, 50 Nanyang Avenue, 639798 Singapore.

Abstract

The recent emergence of Lead halide perovskites as ionic-electronic coupled semiconductors motivates us to investigate alternative solution processable materials with similar modulatable ionic and electronic transport properties. Here we investigate a novel semiconductor – cubic $NaSbS_2$ for ionic-electronic coupled transport through a combined theoretical and experimental approach. The material exhibits mixed ionic-electronic conductivity in inert atmosphere and superionic conductivity in humid air. We show for the first time, post deposition electronic reconfigurability in this material enabled by electric field induced ionic segregation enabling Switchable Photovoltaic effect. Utilizing post-perturbation of ionic composition of the material via electrical biasing and persistent photoconductivity, we realize multi-state memristive synapses with higher-order weight modulations for neuromorphic computing opening up novel applications with such ionic-electronic coupled materials.

Mixed ionic–electronic conductors (MIECs) are materials that can conduct both ions and electronic charge carriers. Although MIECs have been explored for long, interest has grown in recent years due to their applications in electrochemical energy storage materials, bioelectronics, soft robotics, supercapacitors, electrochromics and separation membranes and catalysts[1]. Devices based on MIECs portray several favorable properties such as ionic conductivity, ability to intercalate ions, capacitance changes on ion accumulation and structural and optical changes on ionic diffusion[2]. However, all these devices treat electronic and ionic currents as separate entities without effectively utilizing a possible coupling between these two. An ionic accumulation induced doping which in turn modulates the electronic properties of the semiconductor could open up new applications in electronics. Organic electrochemical transistors (OECTs) rely on a similar principle, ie doping of organic semiconductors by an external ion to change the conductivity[3]. However, in the case of inorganic semiconductors such a doping effect is difficult since the defects which aid ionic transport, typically induce deep traps which hinder electronic transport. Composite approaches of mixing a graphite electronic conductor with a superionic conductor have been explored to achieve

high ionic conductivity together with electronic conductivity, however no coupling between the two phases were noted [4].

The recent emergence of Lead halide perovskites as ionic semiconductors is highly promising in this respect. These ionic materials have revolutionized the field of photovoltaics and light emission due to their excellent electronic and photonic properties. Simultaneously they have found applications in memristive systems[5] and switchable photovoltaics[6,7] due to the coexistence and coupling of ionic and electronic components of current. This co-existence of ionic and electronic properties can be attributed to its defect tolerance – ie the ability of a semiconductor to retain its properties despite the presence of point defects. The presence of ns^2 electrons, a high dielectric constant and the presence of the heavy element for strong spin orbit coupling effect are deemed the fundamental reasons for the defect tolerance[8,9]. In addition, a well-connected soft lattice enabling high electronic and ionic mobility play a major role in determining the ionic conductivity of these mixed conductors. The ionic migration can be assisted by grain boundaries aligned parallel to the flow of ions and impeded by those perpendicular to it[10,11]. The ions which are blocked at the boundaries can help in local doping of the material by creation of shallow traps. These observations form the basis for our investigation into similar materials and setting up design rules to explore ionic electronic coupled semiconductors which can be easily modulated and made into functional devices.

In this report, materials which have higher ionic conductivity compared to halide perovskite but still exhibit defect tolerance were explored to unlock useful applications. Cubic $NaSbS_2$ was identified as a potential candidate and its optoelectronic properties were evaluated through a combined experimental and theoretical approach. A novel facile solution processing strategy was developed to form thin films of this mixed ionic-electronic conductor. This is the first report on a material that can exist as a superionic conductor as well as a semiconductor under suitable conditions. We show for the first time, switchable photovoltaic effect in this chalcogenide semiconductor by electrically re-configuring it after deposition. Finally, utilizing persistent

photoconductivity and perturbation of ionic composition of the material via electrical biasing, we realize multi-state memristive synapses with higher-order weight modulations for neuromorphic computing hence opening up novel applications with such ionic-electronic coupled materials.

Based on the above mentioned initial design rules (Figure 1a), the ICSD database[12] and Materials Project[13] was scanned for viable ternary compounds based on Sb and Bi with ns^2 electrons which possess a highly symmetric and connected structure. Tin, Indium and Germanium were excluded from the search because of their inherent tendency to oxidise and lose the ns^2 electrons. Several compounds including $NaSbS_2$, $LiSbS_2$, $AgSbS_2$, K_3SbS_3, Rb_3SbS_3, $Cu_{12}Sb_4S_{13}$, $NaBiS_2$, $AgBiS_2$, $LiBiS_2$, $KBiS_2$, $AgBiI_4$ and $CuBiI_4$ were identified (Figure S1-S5). Copper and silver containing compounds were eliminated because of their strong contribution to band edges. Presence of the mobile element not contributing to the band edges is necessary to avoid deep defects on migration. Among the remaining candidates, Alkali metal antimony chalcogenides are highly interesting because of their compositional variety[14] and flexibility, high dielectric constants[15], semiconducting nature and the high conductivity of the Alkali metal cation[16,17].

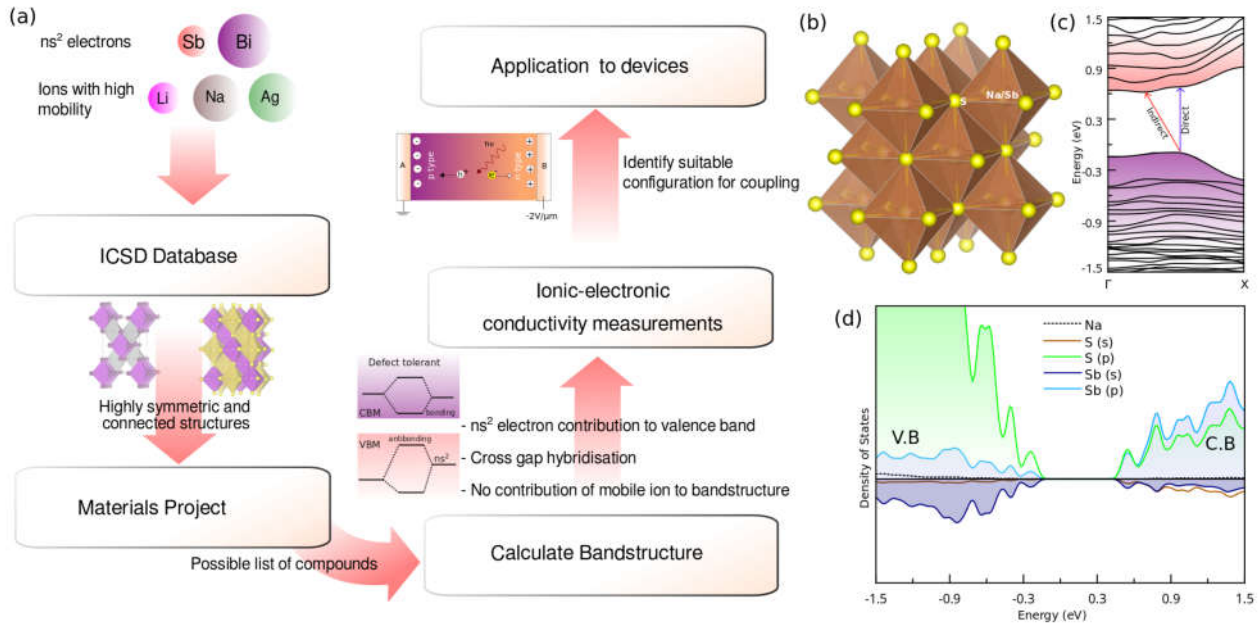

Figure 1: The design rules for selecting ionic-electronic coupled materials, (b) The crystal structure (c) Density of States and (d) Electronic Band structure of cubic $NaSbS_2$

Among these, $NaSbS_2$ is a promising candidate because of its reported semiconducting properties[18]. The material exists in several structures – monoclinic (C 1 2/c 1), triclinic (P -1) and cubic (F m -3 m) and has recently gained attention for solar cell applications[19–22]. Most of the studies have been focused on the disconnected and lower symmetry monoclinic phase of $NaSbS_2$. First principle calculations on monoclinic and triclinic structures show similarity of the band structure with lead halide perovskites[15,23]making it a promising semiconductor with possible defect tolerant properties. Eventhough a symmetric cubic structure[21,24] of this material has been reported, its optoelectronic properties and band structure has not been evaluated in detail. Cubic $NaSbS_2$ forms the focus of this study because of its well connected structure which may enable superior ionic and electronic mobility compared to other phases. The structure of the material as shown in Figure 1(b) is similar to NaCl structure with Na/Sb having partial occupancy. This complicated the DFT analysis since there can be ordered and disordered arrangement for the Na and Sb atoms. To begin with, the cubic (Fm -3m) $NaSbS_2$ with an ordered arrangement of Na and Sb atoms in the lattice was analyzed (Figure S6). The crystal structure was optimized based on the lowest energy configuration. Interestingly, the band structure showed metallic character which is contradictory to the experimental results discussed later in text. On recalculating the band structure with a random arrangement of Na and Sb atoms in the lattice (Figure S7), the band gap increased significantly to 0.71 eV indicating possibility of such an arrangement in the thin films. The density of states calculation (Figure 1c) indicated strong contribution of Sb(s) and S(p) orbitals in the valence band and Sb (p) and S(p) orbitals towards the conduction band edge (Figure 1d). The presence of an anti-bonding valence band maximum results in defects forming only within the valence band without inducing deep traps in the band gap similar to halide perovskites [8]. The cross-gap hybridization between S(p) and Sb (p) can result in high dielectric constants [25] which would further assist defect screening. Furthermore, the material exhibits an indirect band gap with a very close direct transition (Figure 1c). However, the indirect band gap may not be detrimental in this case as the p to p transitions will enable a high absorption coefficient and the indirect recombination may prolong the

carrier lifetimes as observed in antimony-based perovskites [7]. Most importantly, it is seen that Na has negligible contribution to the band edges (Figure 1d). This is quite similar to halide perovskites where the A site cation does not contribute to the band edges. This is very important since the material is expected to show high Na ion conductivity. Since Na does not take part in bonding, motion of the ion will not introduce deep defects in the band gap thus retaining the electronic properties despite slight local changes in Na ion concentration.

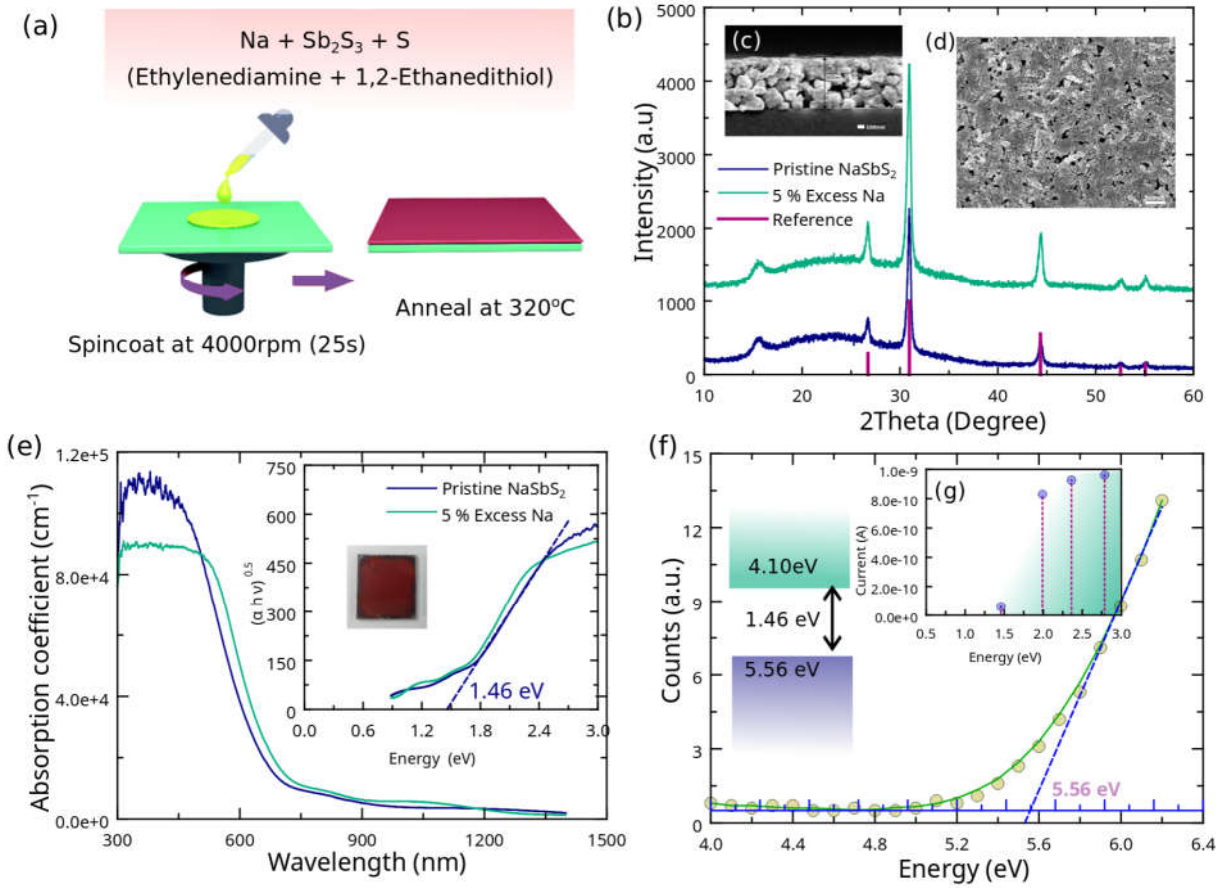

Figure 2: (a) The schematic showing the spincoating procedure for $NaSbS_2$ using the Amine-Thiol route. (b) The XRD pattern of the pristine $NaSbS_2$ film and the film formed with 5% excess Na in the precursor. Insets (c and d) show the the cross-sectional and top view SEM , (e) The absorption coefficient and the Tauc Plot, (f) PESA measurements and (g) The photoconductivity measurements at various wavelengths.

Thin films of $NaSbS_2$ were fabricated by a novel solution processing route by dissolving Sb_2S_3, elemental S and Na in amine-thiol mixtures [26] (Figure 2a). Attempts to form the material using alternative techniques using NaOH, $SbCl_3$ and Thiourea in Dimethylformamide failed and resulted in Sb_2S_3 films (Figure S8). The precursor solution in amine-thiol mixture discussed above can be spin coated to obtain thin films of cubic $NaSbS_2$. X-Ray diffraction pattern of the cubic $NaSbS_2$ matched well with the reference pattern (Figure 2b). The peak at 15.7° could be from (200) peak of Sb_2S_3 or the (113) peak of orthorhombic Sulfur indicating that these might be present as impurity phases in the films. It was observed that this impurity phase becomes more pronounced on annealing at higher temperatures (Figure S9). Organic phases are observed in the sample annealed at a low temperature of 150°C as evident from the presence of C-H and N-H stretches in the FTIR spectrum. However, these are completely removed on annealing at 320°C (Figure S10). The Auger spectrum shows absence of C and N peaks indicating that all organics are completely removed at this temperature. The films were around 800 nm thick and had a mesoporous morphology (Figure 2c,d). The resulting films exhibited higher moisture stability compared to halide perovskites and retained the XRD pattern and absorption spectrum even after dipping in water (Figure S11).

In order to check the compositional flexibility of the material, the effect of excess Na in the precursor solution was studied. Addition of slight excess of Na (5 to 10%) to the solution did not shift the XRD pattern and the morphology (Figure S12). Auger electron Spectroscopy mapping indicates that in both the samples the Na is distributed evenly across the thin film and not segregated at grain boundaries (Figure S13). It was also observed that excess Na is associated with a reduction in the Sb content in the film (Table S1). The material exhibited high absorption coefficients of around 1 x 10^5 cm^{-3} (as expected from theoretical predictions) close to the values reported for lead halide perovskites (Figure 2e). It was seen that a 5% Na excess in the precursor solution did not change the absorption onset significantly. The Tauc plot fitting yields a direct band gap of ~2eV and an indirect band gap of 1.46 eV (Figure S14). Photo current measurements made at different wavelengths, indicated high photocurrents for incident photon energies exceeding 1.5eV

(Figure 2g). This along with the absence of a sharp absorption onset and the theoretical predictions suggest that the band gap is most probably indirect (1.46eV). Photoelectron spectroscopy in air (PESA) measurements (Figure 2f) indicate a valence band edge of 5.56 eV and conduction band edge of 4.1eV which is compatible with most electron and hole extraction layers for use in solar cells.

The opto-electronic response of the material was investigated in a lateral architecture with interdigitated FTO electrodes. The material exhibited significant photo response in vacuum with an on-off ratio of around 10 (Figure 3a). This low on-off ratio might be associated with traps and high ionic conductivity of the sample. In addition, the photo-current exhibited a long decay time (Figure S15) possibly arising from the slow relaxation of the trapped carriers resulting in persistent photoconductivity (PPC). Although, this PPC behaviour may be detrimental in a photovoltaic device or a photodetector, the light induced memory behavior can be positively utilized in artificial photonic synaptic devices as discussed later in text. The electronic properties of the material drastically changed with respect to the ambient with the dark conductivity increasing 3 orders of magnitude on exposure to humid air (Figure 3a). This was accompanied by negligible photo response from the material in the ambient (Figure S16). This increase in dark current was not observed on measuring the sample in dry air indicating the role of moisture on the conductivity of the sample (Figure S17). Our preliminary studies point to increased ionic migration under humidity as a reason for the improved conductivity and reduced photoresponsivity as discussed later in text. Impedance spectroscopy was used separate out the ionic and electronic components of current in the materials using the same lateral FTO electrodes. The ions are conducted through the bulk and blocked at the material/electrode interface whereas the transport of electrons is not. Such an interface can be modeled as a parallel plate capacitor (C_{dl}) combining effects of both the electrodes.

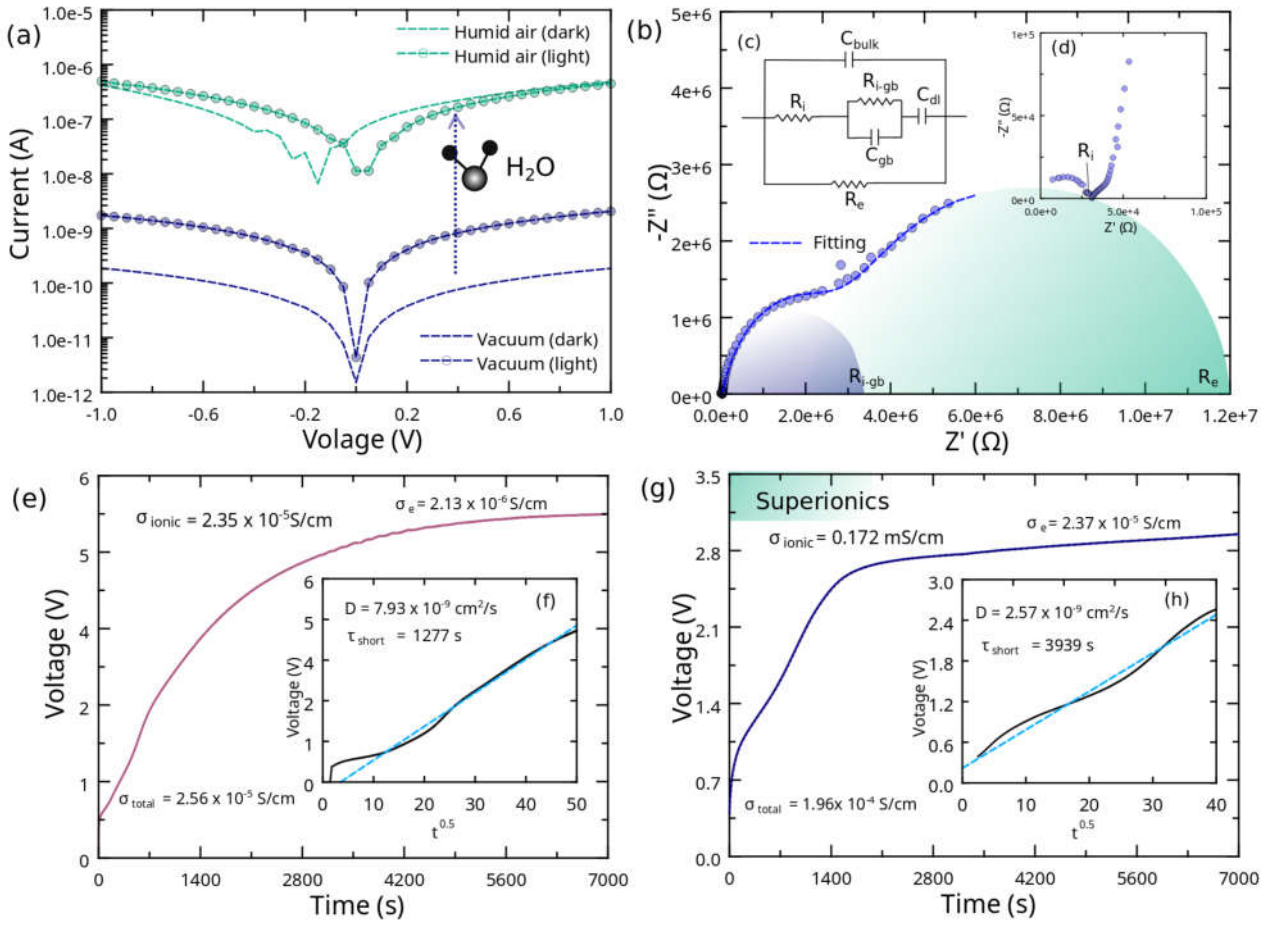

Figure 3 : (a) Dark and photoconductivity of $NaSbS_2$ in Vacuum and Humid Air (445nm, 140mW/cm^2). (b) The impedance spectroscopic measurement for decoupling the ionic and electronic conductivity, The insets (c) and (d) represent the equivalent circuit used to fit the measurement and the high frequency region of the impedance measurement. (e) Galvanostatic measurements on Pristine sample and (g) 5% excess Na sample respectively. The insets (f and h) show the transient fits to the initial short time response of both to extract the diffusion coefficient.

The resultant transport mechanism can be modeled using an equivalent circuit that include components for electronic (R_e) and ionic path (R_i) in parallel. In addition to this, a capacitance (C_{bulk}) acts parallel to the whole configuration due to the dielectric constant of the material [27]. The SEM image indicates a mesoporous structure with a lot of grain boundaries (Figure 2c). In Mixed-Ionic electronic conductors, it is known that the grain boundaries which are transverse to the direction of applied field can impede the motion of ions because of the discontinuity in the

lattice[27] and those which are parallel to the applied field can enhance ionic motion. This is also observed in halide perovskites where ions blocked at grain boundaries lead to local doping effects[7,11]. Hence, the grain boundaries which are perpendicular to the ionic transport will impede the ionic migration and will introduce an additional ionic impedance ($R_{i\text{-}gb}$) that must act in series with the bulk ionic resistance. This is also associated with a parallel local capacitance (C_{gb}). The complete equivalent circuit and the generic curve associated with it is shown in Figure 3b-d. The calculated resistances and the corresponding specific conductivity are listed in Table 1. The bulk ionic conductivity of 2.55 mS/cm indicate superionic conductivity in the material. However, the conductivity is impeded by the grain boundaries which add additional resistance to the motion of ions resulting in an effective ionic conductivity of 2.47 x 10^{-5} S/cm. The effective electronic conductivity was one order less than the ionic conductivity indicating the dominant role of ions in the conduction mechanism. The raw data used for impedance spectroscopy and DC polarization measurements mentioned in the next section is available at https://osf.io/nw9su/ (DOI 10.17605/OSF.IO/NW9SU)

Table 1 : The resistances obtained from Impedance fitting and Galvanostatic measurements for the pristine $NaSbS_2$ in humid air.

Component	**Resistance (ohm)**	**Specific Conductivity S/cm (Impedance)**	**Specific Conductivity S/cm (Galvanostatic)**
$\mathbf{R_i}$	30 x 10^3	2.55 x 10^{-3}	-
$\mathbf{R_{i\text{-}gb}}$	3.1 x 10^6	2.47 x 10^{-5}	2.35 x 10^{-5}
$\mathbf{R_e}$	11 x 10^6	6.96 x 10^{-6}	2.13 x 10^{-6}

The results were corroborated using DC polarization measurements. Sandwiching the mixed ionic electronic conductor (MIEC) in between suitable ion/electron blocking electrodes and under a constant current bias would lead to polarization of the material and development of a potential gradient (known widely as Wagner-Hebb or Yokota polarisation[11]). For purely electronic conducting (ion blocking) electrodes, there is an initial potential which gradually saturates with time. At the point of saturation, only the electrons contribute to the conductivity (σ_{e0}) whereas at the instant of

switching on the current, both electrons and ions contribute ($\sigma_{i0} + \sigma_{e0}$). The ionic conductivity of the sample in humid air (Figure 3e) calculated from this relation (2.35 x 10^{-5} S/cm) is one order of magnitude higher than its electronic conductivity (2.13 x 10^{-6} S/cm) which is very close to the values obtained from the impedance spectroscopy. The investigation of the voltage transients prove that the observed polarization is caused by a chemical diffusion. As in case of chemical diffusion, the transient fits a $\sqrt{t}$ law for short times (Figure 3f and h) and exponential behavior for longer time (Figure S18 and S19). Both these time dependencies were verified from the excellent match of the time constants of 1277 s and 1418 s. The chemical diffusion coefficient of the ion ($D= L^2/(\pi\tau)$ where L is the distance between two electrodes) is calculated to be 7.93 x 10^{-9} cm^2/s. If sodium ions are responsible for the conduction mechanism, excess Na in the precursor solution should lead to films with enhanced ionic conductivity. The effective ionic conductivity of sample with 5% excess Na was found to be 0.17 mS/cm which is one order higher than the pristine sample (Figure 3g). This value is one of the highest reported for any thin film sodium ion conductors indicating their potential application in solid electrolytes for thin film batteries[16,28–30]. Significantly, the diffusion coefficient of the sample with 5% Na excess (2.57 x 10^{-9} cm^2/s) was of the similar order as that observed for the pristine sample indicating that the improved ionic conductivity is caused by excess available ions rather than improved diffusion. Interestingly in vacuum, the curve do not saturate even after 8 hours indicating slow diffusion. The approximate ionic (3.55 x 10^{-9} S/cm) and electronic conductivity (1.6 x 10^{-9} S/cm) are four orders lower than that observed in humid air (Figure S20 and Table 2). The low ionic diffusion coefficients (8 x $10^{-10}$$cm^2/s$) calculated from the short time response indicate that the diffusion of ions is moisture driven (Figure S21). This reduction of dark electronic conductivity could be due to reduction in density of trap states in the form of free ions in the film. Hence, the material is unique by being an ionic conductor in presence of moisture and a semiconductor with coupled ionic transport under dry atmosphere. This tunable ionic electronic transport facilitates the facile coupling of both phases for application in functional devices.

Table 2 : Comparison of Conductivity and diffusion coefficients of Pristine and 5% excess Na samples from galvanostatic measurements

Sample	Electronic Conductivity (S/cm)	Ionic Conductivity (S/cm)	Diffusion Coefficient (cm^2/s)
Pristine $NaSbS_2$ (Humid Air)	2.13×10^{-6}	2.35×10^{-5}	7.93×10^{-9}
5% excess Na (Humid Air)	2.37×10^{-5}	1.7×10^{-4}	2.57×10^{-9}

The electrical measurement in vacuum indicated that the IV curves of the material slowly drifted away from the origin on repeated measurements. Similar effects are observed in halide perovskites and is attributed to ionic migration induced doping of the material which enables phenomena like switchable photovoltaic effect [6]. Owing to the moderate ionic conductivity of the material in vacuum, we investigated switchable photovoltaic effects in the material in vacuum by poling to create the ionic drift. The unpoled $NaSbS_2$ film showed linear IV characteristics passing through origin demonstrating ohmic behavior. The device was then poled by application of -2V/um to electrode B under illumination by a Blue LED (445nm) with a power of 1.4 mW/mm^2 for 200s (Figure 4a). The IV curves after removing the negative poling resulted in a positive photo-current from B to A with an open circuit voltage of around 0.2V (Figure 4b and c). The direction of photo-current and voltage flipped on positive poling at B resulting in a switchable direction of photocurrent. The photocurrent is stable and exhibits quick response to light pulses at zero applied voltage. Similar effects were also observed in ferroelectric materials like $BiFeO_3$[31]. However, $NaSbS_2$ is cubic with a center of symmetry, hence ferroelectricity can be ruled out in this material because absence of center of symmetry is an essential criterion for Ferroelectricity. So, the effect must be related to ion migration induced doping as observed in lead halide perovskites. Possibly, the positive Na ions drift to the negatively poled electrode to n-dope the material leading to the formation of an intrinsic p-n junction capable of driving the electrons even in the absence of electron and hole transporting layers. This hypothesis is supported by the recent theoretical studies

on $NaSbS_2$ (in a lower symmetry P1 structure) showing the low formation energy of Na_i which can act as donor defects to n-dope the material[23]. The Energy Dispersive X-ray Scattering (EDS) data shows lower concentration of Na near positively poled electrode supporting this hypothesis (Figure S22). The extraction of charges despite the long electrode spacing of 100µm indicate good carrier diffusion lengths in the material. For better investigation of the phenomenon, the lateral devices were subjected to varying poling field and poling duration. It was seen that the induced current increased and saturated with the poling time (Figure 4d). Similar behavior has been observed in Lead [6] and Antimony [7] based perovskites and is a typical characteristic of ion migration where the migrating ions reach an equilibrium after a particular time.

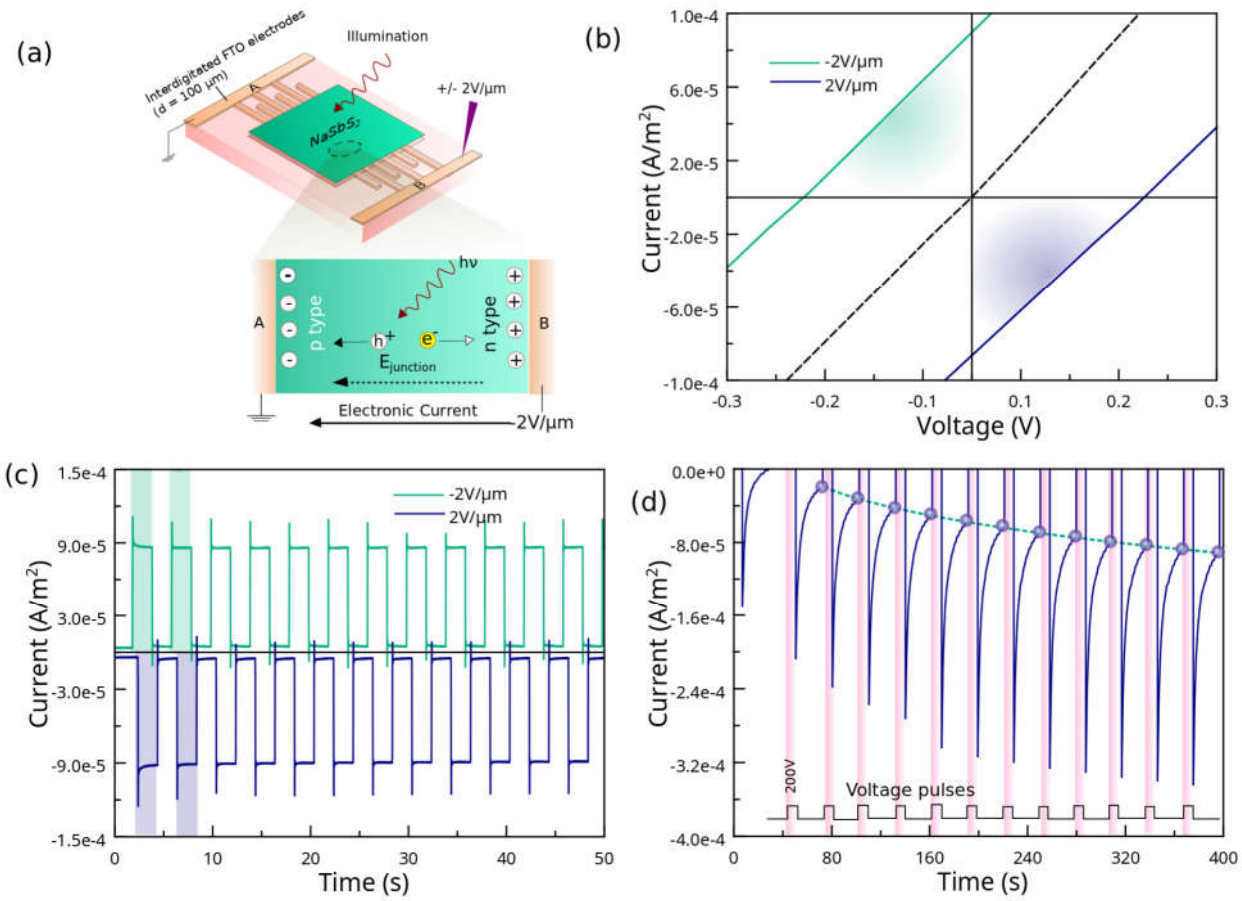

Figure 4 : (a) Schematic of the device configuration for SPV study, (b) Switchable Photovoltaic behavior developed after electrical poling, (c) the response of the poled devices to pulsed light and

(d) the temporal change in the short circuit current developed inside the material on poling by voltage pulses

Intensity dependent studies also pointed to accumulation of ions at the interfaces leading to space charge effects in the sample (Figure S23). The ion induced doping coupled with the persistent photo-conductivity of the material is utilized to demonstrate an artificial synaptic device.

Synapse is the connection between two neurons (pre and post neurons) in the brain and permits the transfer of information in the form of electrical/chemical signal. The presence of slowly decaying current/voltage signals induced by an input pulse (electric or optical) and history dependent output signals are the fundamental requirements for an artificial synapse[5,32,33]. In this device, the light pulse is the presynaptic input and the current across the two lateral FTO electrodes is the post-synaptic output (Figure 5a). A presynaptic input (Optical pulse of 35 mW/cm^2, 445nm) under a constant applied bias of 1V triggers an Excitatory post-synaptic current (EPSC) in the channel (Figure 5b). The EPSC reaches a peak value of 23pA which decays slowly on removal of the spike to the resting current of 14 pA in around 15 seconds. This EPSC behavior is quite similar to an EPSC process in a biological synapse. The energy consumption per single pulse event is only 5.75 pJ (given by I_{peak} x t x V) and shows potential to reduce the energy consumption to femto joule levels on reduction of pulse width. The synaptic weight gradually decays over time and based on its lifetime, it can be categorized as Short-term synaptic plasticity (STP) or Long-term synaptic plasticity (LTP). Plasticity occurs in multiple time scales in human brain- while long-term plasticity happening on a time scale of several minutes is believed to be the cause of experience-dependent alteration of the neural circuit, short-term plasticity occurring on a time scale of tens of milliseconds is beneficial for temporal filtering and could play a role in speech processing and working memory [5,33,34].

To modulate the plasticity behavior, different illumination intensities were applied to the device (Figure S24). It was seen that the synaptic weights increased on application of a higher intensity photonic pulse. With a low intensity (35mW/cm^2) light pulse, the current reduced back to

its original state in around 15s which is quite similar to STP. When the intensity was increased to 840mW/cm^2 , the synaptic weight change persisted at a higher level showing potential to transition to LTP. This means the device can be shifted from an STP behavior to LTP behavior just by adjusting the intensity of the light pulse. Increasing the driving voltage from 1V to 3V did not however lead to an increased weight change (Figure S25).

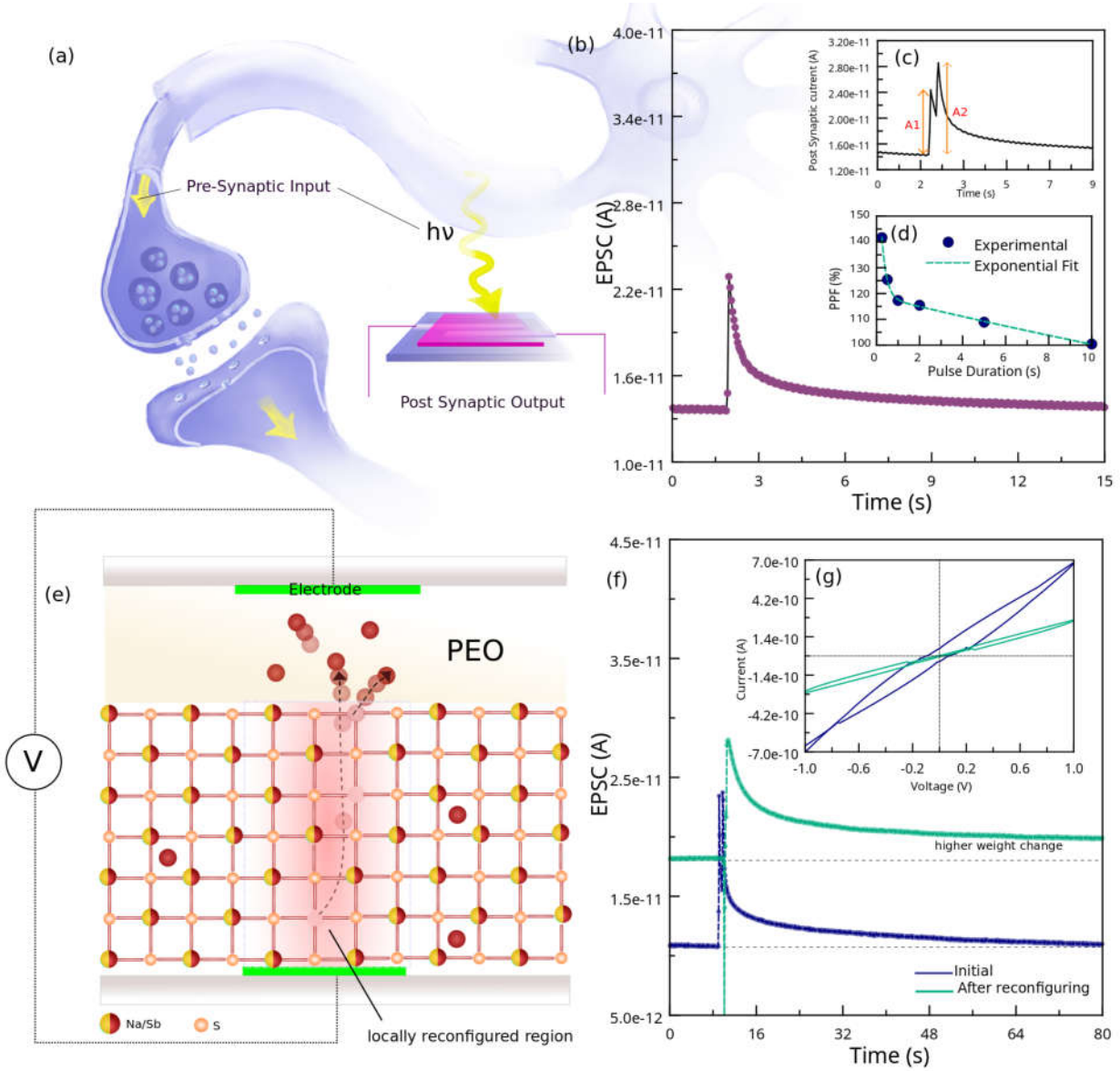

Figure 5 : (a) Schematic of the operation of a biological synapse and the analogous artificial synapse, (b) EPSC after a single and (c) multiple pulses. (d) PPF index variation with the increasing interval. (PPF index is the ratio between second (A2) and first (A1) post synaptic current). (e)

Device structure used for electrical reconfiguration study (f) The EPSC before and after re-configuring $NaSbS_2$ and (g) The IV curves before and after re-configuring by removing Na ions.

Paired pulse facilitation (PPF) is a phenomenon in which EPSC induced on the first spike is increased when the second spike closely follows it. PPF is thus a form of short-term synaptic plasticity and is required to decode temporal information in the biological system. This PPF behaviour can be successfully emulated in this artificial synaptic device. The current in the artificial synaptic device increased when a pair of successive optical signals were applied as required in case of a biological synapse (Figure 5c). The paired-pulse facilitation ratio (PPF) is the ratio of A_2 to A_1 where A_2 and A_1 are the current levels corresponding to the optical spikes. The PPF indices varied inversely with the pulse intervals with short pulse intervals (250ms) yielding high PPF indices. PPF index reached 100% for around 10000ms (Figure 5d). Similar to the coupling of biological neurons, this behavior fits well with an exponential decay :

$$y = B_1 \cdot \exp\left(\frac{x}{t_1}\right) + B_2 \cdot \exp\left(\frac{x}{t_2}\right) + y_0$$

where x is the pulse interval, y0 is the facilitation magnitude, B1 and B2 are facilitation constants, t_1 and t_2 are the characteristic time constants associated with it. The time constants t_1 and t_2 were calculated to be 0.18 s and 5.67 s respectively. The material also exhibits synaptic behavior in the presence of purely electrical input utilizing the back diffusion of ions as shown in Figure S26 albeit with lower time constants 1.62ms and 137.2ms respectively.

From the band structure, it is clear that Sodium ion do not significantly contribute to the band edges and hence incorporation or removal of sodium ions should not greatly deteriorate the electronic properties of this material. As discussed previously, an increase in sodium content can improve the ionic conductivity of the sample and also potentially help in doping the sample. This opens up the possibility to remove some sodium ions from a deposited film by using an electric field to an ionic drain thus altering the electronic properties of the material after deposition. In order to investigate this, a Polyethylene Oxide (PEO) coated FTO substrate with was integrated on top of the lateral device used for the artificial synapse study (Figure 5e). Slight heating of the device at

70°C helped to melt the PEO thus forming intimate contact with $NaSbS_2$. The synaptic device was tested before and after electrical re-configuration of the material (Figure 5f). The initial IV curve across the lateral electrodes show high hysteresis which is common for highly ionic conducting materials (Figure 5g). The device was then electrically poled vertically by applying a voltage of 20V for 200s to the PEO side in order to extract the Na ions to the PEO layer (Figure 5e). This resulted in a significant reduction in hysteresis in the dark currents (Figure 5g) of the sample possibly because of the reduction in concentration of free interstitial Sodium in the sample. Initially the post-synaptic current decayed fast showing an STP behavior. Upon reconfiguration, the device retained significant weight change even after 80s indicating transition to LTP behavior showing the potential to tune the material by electrical reconfiguration (Figure 5f). Given, the spatial non uniformity across several synaptic devices is one of the major problems for developing practical neuromorphic circuits, this strategy of actively modulating the ionic and electronic properties of the material after fabrication by electrical poling offers a potential solution to tackle the issue by correcting the synaptic weights on demand.

In summary, a novel electrically re-configurable chalcogenide semiconductor – $NaSbS_2$ was designed and synthesized for applications such as in switchable photovoltaic and neuromorphic computing. A facile solution processing strategy was developed to form thin films of the material in its cubic structure. The high electronic dimensionality and similarity in density of states of the material to lead halide perovskites equips it with defect tolerance and enables ionic-electronic coupled transport in the material. The material exhibits mixed ionic electronic conductivity in inert atmosphere and super-ionic conductivity in ambient atmosphere. The mixed-ionic electronic conductivity in inert atmosphere was utilized to electrically post process the material to induce switchable photovoltaic effects and short and long-term plasticity in artificial synapses. The insights from the study are not limited to $NaSbS_2$ but to other Alkali metal Antimony and Bismuth dichalcogenides which can be formed easily by the reported approach.

Experimental Section

Density Functional Theory Calculations : Electronic structure calculations are carried out based on Generalized Gradient Approximation (GGA) of Density Functional Theory (DFT) using Perdew-Burke-Ernzerhof (PBE) exchange correlation functional as implemented in Vienna Ab-initio Simulation Package (VASP)[35–40]. Projector Augmented-Wave (PAW) pseudopotentials were used to describe the valence state and the interaction between electrons and ions. A Gamma-centered Brillouin zone integration with 5x5x5 meshes for 2x2x2 supercell and 450 eV as cut-off energy were used for structural optimization and electronic properties calculations.

Thin film formation: Solutions were prepared by dissolving Na , Sb_2S_3 and S in 1ml ethylene diamine and 0.1ml ethanedithiol to get a 1M solution at room temperature for 3 hours. The solution was then spin coated at 2000rpm for 30s followed by annealing at 250ºC for 10 minutes. To form thicker films, the process was repeated several times with a final 320ºC annealing for 30 minutes. Annealing at higher temperatures above 320°C and more than 1 hour did not improve the crystallinity of the film as evident from the XRD (Figure S9b, S27). It was observed that on dropping the solution to the first layer, the film becomes transparent and redissolves. Hence a dynamic spinning was adopted with the solution dropped on the spinning substrate. Annealing in presence of sulfur vapour transformed the structure to a lower symmetry phase (Figure S28). Very high Na (20% and 40%) content in the precursor solution lead to highly amorphous samples which are highly moisture sensitive with poor optoelectronic properties (Figure S29-S31).

Structural and Optical characterisation: The powder XRD patterns were obtained on Bruker D8 Advance diffractometer in Bragg-Brentano configuration with Cu Kα X-Rays of wavelength 1.54187 Å at 40kV and 40mA. The thin films were characterized at a step size of 0.05° and stepping time of 1s. The sample stage was rotated to compensate for non-uniformities in film. The absorption, reflectance and transmittance spectra were obtained using a UV–vis spectrometer (SHIMADZU UV-3600 UV–vis-NIR Spectrophotometer) with an integrating sphere (ISR-3100).

Auger electron spectroscopy (AES) was performed with a field-emission Auger microprobe (JEOL JAMP-7830F) with a primary electron beam having an accelerating voltage of 10 keV and a

probe current of 10 nA. The sample was tilted at 30° throughout the analysis and the analysis area for spectroscopy was approximately 75 x 75 μm^2 (equivalent to 2000x magnification). Auger mapping was collected from an area of 15 x 15 μm^2 corresponding to magnification of 20,000x), with a dwell time of 5 ms and averaged over 5 accumulations. The analyser was operated at a constant retarding ratio (CRR) mode (energy resolution < 0.5%) for both spectroscopy and mapping. The surface composition was determined by considering the peak-to-peak distance of the differentiated Auger spectra and the relative sensitive factor (RSF) for the elements of interest, i.e., Na, Sb and S.

Switchable photovoltaic effect measurements: Interdigitated FTO elctrodes (3 Fingers) with lateral spacing of 100µm and total effective length of 3.17cm was used in fabrication of lateral device as shown in Figure 4a. The active material (800nm thick) was spincoated as reported in the Thin film formation section.The measurements were conducted in a probe station chamber under vacuum of 10^{-3} mbar with the light incident through a quartz window. A monochromatic blue LED of wavelength 445nm and power 1400W/m^2 was used for poling as well as the photocurrent measurements. Electrical properties were measured using a Keithley 4200-SCS semiconductor characterization system. The electric field applied on the perovskite film is 2V/µm for 200s under illumination by Blue LED. After poling, the IV and I-t curves were measured using the Keithley 4200-SCS.

Neuromorphic device characterization : The devices were of the same configuration as used for the switchable photovoltaic effect measurements. The current between two lateral electrodes A and B form the post synaptic output and the light pulse to the device is the pre synaptic input. The ionic electronic coupling and the persistent photo conductivity of the material are utilized to emulate synaptic functions. The light pulses are provided using a blue LED (445nm) with varying power and the electrical characteristics are measured using Keithley 4200-SCS. For the weight change analysis the following approach is used in the work (1) Read the device conductance with an applied bias voltage. This voltage is varied to achieve the required initial conductance.(2) Apply the

Photonic pulse of required power and monitor the transient change in conductance. The power of the pulse, number and pulse duration are varied to obtain the required STP or LTP behavior. (3). Monitor the conductance state after 80s after the pulse and compare it with the initial conductance state to obtain the weight change. (4) PPF index is calculated as the ratio of the peak conductance on application of the subsequent photonic pulse to the first pulse.

For electrically re-configuring the synaptic device, FTO electrode with drop casted PEO was integrated on top of the lateral device and heated to 70ºC to melt the PEO and form intimate contact with $NaSbS_2$. Poling was done applying -20V for 200s to the FTO electrode to extract the Na ions to the PEO layer.

Acknowledgements

This work was funded by National Research Foundation (NRF), Singapore through the CRP programme (NRF-CRP14-2014-03) and the Intra-CREATE Collaborative Grant (NRF2018-ITC001-001). Funding from Ministry of education Singapore through MOE2016-T2-1-100 and MOE2018-T2-2-083 are also acknowledged. Funding from Office of Naval Research Global (ONRG-NICOP-N62909-17-1-2155) is also acknowledged. We gratefully acknowledge Dr Sudhanshu Shukla's help in the initial preparation of sulphurised samples.

References

[1] P. J. Gellings, *Handbook of Solid State Electrochemistry*, CRC Press, **2019**.

[2] H. L. Tuller, *Solid State Ionics* **1997**, *94*, 63.

[3] X. Wu, A. Surendran, J. Ko, O. Filonik, E. M. Herzig, P. Müller□Buschbaum, W. L. Leong, *Advanced Materials* **2019**, *31*, 1805544.

[4] C.-C. Chen, L. Fu, J. Maier, *Nature* **2016**, *536*, 159.

[5] R. A. John, N. Yantara, Y. F. Ng, G. Narasimman, E. Mosconi, D. Meggiolaro, M. R. Kulkarni, P. K. Gopalakrishnan, C. A. Nguyen, F. D. Angelis, S. G. Mhaisalkar, A. Basu, N. Mathews, *Advanced Materials* **2018**, *30*, 1805454.

[6] Z. Xiao, Y. Yuan, Y. Shao, Q. Wang, Q. Dong, C. Bi, P. Sharma, A. Gruverman, J. Huang, *Nature Materials* **2015**, *14*, 193.

[7] P. C. Harikesh, B. Wu, B. Ghosh, R. A. John, S. Lie, K. Thirumal, L. H. Wong, T. C. Sum, S. Mhaisalkar, N. Mathews, *Advanced Materials* **2018**, *30*, 1802080.

[8] R. E. Brandt, V. Stevanović, D. S. Ginley, T. Buonassisi, *Mrs Communications* **2015**, *5*, 265.

[9] M. H. Du, *J. Mater. Chem. A* **2014**, *2*, 9091.

[10] Y. Shao, Y. Fang, T. Li, Q. Wang, Q. Dong, Y. Deng, Y. Yuan, H. Wei, M. Wang, A. Gruverman, J. Shield, J. Huang, *Energy Environ. Sci.* **2016**, *9*, 1752.

[11] Y. Yuan, T. Li, Q. Wang, J. Xing, A. Gruverman, J. Huang, *Science Advances* **2017**, *3*, e1602164.

[12] "ICSD: ICSD Web," can be found under http://www2.fiz-karlsruhe.de/icsd_web.html, **n.d.**

[13] A. Jain, S. P. Ong, G. Hautier, W. Chen, W. D. Richards, S. Dacek, S. Cholia, D. Gunter, D. Skinner, G. Ceder, K. A. Persson, *APL Materials* **2013**, *1*, 011002.

[14] M. G. Kanatzidis, D. Y. Chung, C. R. Kannewurf, T. Hogan, L. Iordanidis, *Alkali Metal Chalcogenides of Bismuth Alone or with Antimony*, **2000**, US6013204A.

[15] J. Sun, D. J. Singh, *Phys. Rev. Applied* **2017**, *7*, 024015.

[16] S. Xiong, Z. Liu, H. Rong, H. Wang, M. McDaniel, H. Chen, *Scientific Reports* **2018**, *8*, 9146.

[17] C. Pompe, A. Pfitzner, *Zeitschrift für anorganische und allgemeine Chemie* **2012**, *638*, 2158.

[18] V. A. Bazakutsa, N. I. Gnidash, A. K. Kul'chitskaya, A. V. Salov, *Soviet Physics Journal* **1975**, *18*, 472.

[19] S. U. Rahayu, C.-L. Chou, N. Suriyawong, B. A. Aragaw, J.-B. Shi, M.-W. Lee, *APL Materials* **2016**, *4*, 116103.

[20] W.-C. Sun, S. U. Rahayu, M.-W. Lee, *IEEE Journal of Photovoltaics* **2018**, *8*, 1011.

[21] Z. Xia, F.-X. Yu, S.-C. Lu, D.-J. Xue, Y.-S. He, B. Yang, C. Wang, R.-Q. Ding, J. Zhong, J. Tang, *Chinese Chemical Letters* **2017**, *28*, 881.

[22] W. W. Winnie Leung, C. N. Savory, R. G. Palgrave, D. O. Scanlon, *Journal of Materials Chemistry C* **2019**, *7*, 2059.

[23] X. Zhang, M. Huang, P. Xu, C.-M. Dai, Z.-H. Cai, D. Han, S. Chen, *Progress in Natural Science: Materials International* **2019**, DOI 10.1016/j.pnsc.2019.02.009.

[24] J. Olivier□Fourcade, E. Philippot, M. Maurin, *Zeitschrift für anorganische und allgemeine Chemie* **1978**, *446*, 159.

[25] X. He, D. J. Singh, P. Boon-on, M.-W. Lee, L. Zhang, *J. Am. Chem. Soc.* **2018**, *140*, 18058.

[26] D. H. Webber, R. L. Brutchey, *J. Am. Chem. Soc.* **2013**, *135*, 15722.

[27] R. A. Huggins, *Ionics* **2002**, *8*, 300.

[28] A. Banerjee, K. H. Park, J. W. Heo, Y. J. Nam, C. K. Moon, S. M. Oh, S.-T. Hong, Y. S. Jung, *Angewandte Chemie International Edition* **2016**, *55*, 9634.

[29] Z. Zhang, E. Ramos, F. Lalère, A. Assoud, K. Kaup, P. Hartman, L. F. Nazar, *Energy & Environmental Science* **2018**, *11*, 87.

[30] S. Takeuchi, K. Suzuki, M. Hirayama, R. Kanno, *Journal of Solid State Chemistry* **2018**, *265*, 353.

[31] T. Choi, S. Lee, Y. J. Choi, V. Kiryukhin, S.-W. Cheong, *Science* **2009**, *324*, 63.

[32] S. Ambrogio, P. Narayanan, H. Tsai, R. M. Shelby, I. Boybat, C. di Nolfo, S. Sidler, M. Giordano, M. Bodini, N. C. P. Farinha, B. Killeen, C. Cheng, Y. Jaoudi, G. W. Burr, *Nature* **2018**, *558*, 60.

[33] R. A. John, N. Tiwari, C. Yaoyi, Ankit, N. Tiwari, M. Kulkarni, A. Nirmal, A. C. Nguyen, A. Basu, N. Mathews, *ACS nano* **2018**, *12*, 11263.

[34] T. Chang, S.-H. Jo, W. Lu, *ACS Nano* **2011**, *5*, 7669.

[35] G. Kresse, J. Hafner, *Physical Review B* **1993**, *47*, 558.

[36] G. Kresse, J. Hafner, *Physical Review B* **1994**, *49*, 14251.

[37] G. Kresse, J. Furthmüller, *Phys. Rev. B* **1996**, *54*, 11169.

[38] G. Kresse, D. Joubert, *Physical Review B* **1999**, *59*, 1758.

[39] J. P. Perdew, K. Burke, Y. Wang, *Physical Review B* **1996**, *54*, 16533.

[40] J. P. Perdew, K. Burke, M. Ernzerhof, *Physical review letters* **1996**, *77*, 3865.